Mon. Not. R. Astron. Soc. **000**, 000–000 (0000) Printed 19 June 2014 (MN LATEX style file v2.2)

Low-metallicity star formation: Relative impact of metals and magnetic fields

Thomas Peters[1⋆], Dominik R. G. Schleicher[2], Rowan J. Smith[3], Wolfram Schmidt[2], and Ralf S. Klessen[3]

[1] *Institut für Computergestützte Wissenschaften, Universität Zürich, Winterthurerstrasse 190, CH-8057 Zürich, Switzerland*
[2] *Georg-August-Universität, Institut für Astrophysik, Friedrich-Hund-Platz 1, D-37077 Göttingen, Germany*
[3] *Universität Heidelberg, Zentrum für Astronomie, Institut für Theoretische Astrophysik, Albert-Ueberle-Str. 2, D-69120 Heidelberg, Germany*

19 June 2014

arXiv:1406.0346v1 [astro-ph.GA] 2 Jun 2014

ABSTRACT

Low-metallicity star formation poses a central problem of cosmology, as it determines the characteristic mass scale and distribution for the first and second generations of stars forming in our Universe. Here, we present a comprehensive investigation assessing the relative impact of metals and magnetic fields, which may both be present during low-metallicity star formation. We show that the presence of magnetic fields generated via the small-scale dynamo stabilises the protostellar disc and provides some degree of support against fragmentation. In the absence of magnetic fields, the fragmentation timescale in our model decreases by a factor of ~ 10 at the transition from $Z = 0$ to $Z > 0$, with subsequently only a weak dependence on metallicity. Similarly, the accretion timescale of the cluster is set by the large-scale dynamics rather than the local thermodynamics. In the presence of magnetic fields, the primordial disc can become completely stable, therefore forming only one central fragment. At $Z > 0$, the number of fragments is somewhat reduced in the presence of magnetic fields, though the shape of the mass spectrum is not strongly affected in the limits of the statistical uncertainties. The fragmentation timescale, however, increases by roughly a factor of 3 in the presence of magnetic fields. Indeed, our results indicate comparable fragmentation timescales in primordial runs without magnetic fields and $Z > 0$ runs with magnetic fields.

1 INTRODUCTION

The formation of stars at low metallicities, and in particular the determination of their characteristic mass scales, is a central problem in cosmology. Low-metallicity star formation is particularly important during the epoch of reionization, where UV photons from low-metallicity stars turn the intergalactic medium from a neutral into an ionised state (Shapiro et al. 1994; Gnedin 2000; Barkana & Loeb 2001; Schleicher et al. 2008). If their mass is sufficiently low, they may survive until today and serve as observational probes via near-field cosmology (e.g. Clark et al. 2011a,b). Indeed, a number of extremely metal poor stars (EMPs) has been discovered in the Milky Way and in nearby dwarf galaxies (e.g. Frebel et al. 2010; Salvadori et al. 2010; Caffau et al. 2013), including the close-to-primordial star SDSS J1029151+172927 with $Z < 10^{-5}$ $Z_\odot$ at the heart of the Lion (Caffau et al. 2011, 2012).

From a theoretical point of view, the purely primordial stars were considered to be rather massive, with extreme scenarios reaching several hundred solar masses (Abel et al. 2002; Bromm et al. 2002; Yoshida et al. 2008). More recent studies have indicated the possibility of fragmentation (e.g. Clark et al. 2008, 2011a,b; Stacy et al. 2010; Greif et al. 2011, 2012; Smith et al. 2011; Latif et al. 2013c). In addition, radiative feedback appears to set a characteristic mass scale of ~ 50 $M_\odot$ (Hosokawa et al. 2011; Susa 2013). However, these mass scales show significant fluctuations. For instance, large samples consisting of 100 minihalos may also include stars with up to 1000 $M_\odot$ (Hirano et al. 2014), while some halos with particularly high angular momentum or a large degree of turbulence may host stars with less than 1 $M_\odot$ (Clark et al. 2011a; Stacy & Bromm 2014). In more massive primordial halos exposed to strong radiation backgrounds, supermassive protostars with up to 10^5 $M_\odot$ may form (Latif et al. 2013b). A low-mass star formation mode can be obtained during the merger of primordial minihalos, as shocks enhance the electron fraction and the formation of H_2 and HD (Bovino et al. 2014a). A significant spread of the stellar mass scales thus appears to be present already in the primordial case.

In the presence of heavy elements, the cooling of the gas becomes more efficient, thus decreasing the Jeans mass as well as the accretion rate. One thus typically expects a decrease in the characteristic mass scales. Bromm & Loeb (2003) suggested that such a transition occurs at a metallicity of $\sim 10^{-3}$ $Z_\odot$ to $\sim 10^{-4}$ $Z_\odot$, where cooling through

© 0000 RAS

carbon and oxygen lines becomes efficient. At the same time, cooling through dust grains can be important even for dust-to-gas ratios of $\sim 10^{-5}$ times the ratio in the solar neighborhood, potentially triggering fragmentation in close-to-primordial environments (Schneider et al. 2003). Indeed, this mechanism was potentially important for the formation of SDSS J1029151+172927, the extremely metal poor star at the heart of the Lion (see e.g. Schneider et al. 2012; Klessen et al. 2012). The impact of cooling through metal lines and dust has also been explored in detailed one-zone models by Omukai et al. (2005, 2008) and Safranek-Shrader et al. (2010), while Cazaux & Spaans (2004, 2009) and Latif et al. (2012) have demonstrated the importance of H_2 formation on dust grains, which can strongly influence the thermal evolution at metallicities of $\sim 10^{-4}\ Z_\odot$. Detailed three-dimensional (3D) simulations following the impact of dust cooling during gravitational collapse further have shown that the thermal evolution in 3D can deviate from the results found in one-zone models, in particular if the collapsing clouds are rotating (Dopcke et al. 2011, 2013). Simulations exploring low-metallicity star formation for metallicities up to $10^{-2}\ Z_\odot$ for number densities till $100\,\mathrm{cm}^{-3}$ have further been pursued by Jappsen et al. (2007, 2009a,b); Smith et al. (2009); Hocuk & Spaans (2010) and Aykutalp & Spaans (2011).

All in all, the equation of state resulting from the cooling processes discussed here therefore influences the characteristic mass scale of the clumps (Li et al. 2003), as well as the formation of filaments (Peters et al. 2012). In particular in simulations employing a high resolution per Jeans length, it is important that not only the cooling processes are accurately employed, but also that high-order numerical solvers are used when solving the rate equations (Bovino et al. 2013, 2014b). The publicly available package KROME[1] for the modeling of chemistry with such high-order solvers was recently released by Grassi et al. (2014). While such a detailed modeling is certainly desirable in the future, we aim here to reproduce only the main features induced by the cooling, and will therefore adopt a parametrised equation of state derived from the 3D calculations by Dopcke et al. (2013). Using a similar technique, Safranek-Shrader et al. (2014b) have recently followed the formation of the first stellar cluster due to metal line cooling, including the formation of a low-mass star (Safranek-Shrader et al. 2014a). The metallicities required for these scenarios can be reached via supernova feedback from previous generations (e.g. Greif et al. 2008, 2010; Ritter et al. 2012; Wise et al. 2012; Seifried et al. 2014).

While the metallicity is certainly important in regulating the stellar mass scale, it has been speculated early that also magnetic fields may have a strong impact on star formation in the high-redshift Universe (e.g. Pudritz & Silk 1989; Tan & Blackman 2004; Silk & Langer 2006). A central question concerns however their initial field strength, which is highly uncertain in primordial scenarios (Grasso & Rubinstein 2001). Seed fields can be provided through a number of astrophysical mechanisms (e.g. Biermann 1950; Schlickeiser 2012; Schlickeiser & Felten 2013; Shiromoto et al. 2014). A particularly efficient amplification mechanism for initially weak seeds is the small-scale dynamo, a process producing strong tangled fields within a few eddy-turnover times (Schekochihin et al. 2002; Brandenburg & Subramanian 2005; Federrath et al. 2011a; Schober et al. 2012b; Schleicher et al. 2013). This process was therefore suggested to provide strong magnetic fields during the formation of the first stars and galaxies (Arshakian et al. 2009; Schleicher et al. 2010; Sur et al. 2010; de Souza & Opher 2010; Schober et al. 2012a; Sur et al. 2012; Turk et al. 2012; Latif et al. 2013d). In the case of large-scale coherent magnetic fields, Machida et al. (2006, 2008) have shown that they can lead to the suppression of fragmentation and the formation of the first jets in the Universe. More recently, they have provided an in-depth investigation regarding the interplay of the magnetic field with fragmentation and the transport of angular momentum (Machida & Doi 2013), while Latif et al. (2014) have shown that magnetic fields generated via the small-scale dynamo can help to suppress fragmentation during the formation of supermassive black holes.

So far, there is however no study concerning the impact of magnetic fields for low-metallicity star formation, i.e. with metallicities above zero. Here, we provide the first exploration of the combined impact of cooling through metals and dust in the presence of strong tangled magnetic fields, as provided via the small-scale dynamo. Our simulation setup is presented in section 2, while the results are analysed and described in section 3. A summary and discussion is provided in section 4.

2 SIMULATIONS

We present three-dimensional magnetohydrodynamical (MHD) collapse simulations, using the adaptive-mesh code FLASH (Fryxell et al. 2000) and an MHD solver that preserves positive states (Bouchut et al. 2007; Waagan 2009). The initial conditions for our simulations are similar to the ones in Peters et al. (2012). We use a minihalo from a cosmological simulation of Greif et al. (2011). This halo corresponds to Halo 4 in their nomenclature and has a virial mass of $3.1 \times 10^5\,\mathrm{M}_\odot$ and a virial radius of 97 pc. Once the halo has collapsed to a central density of $2.8 \times 10^{-15}\,\mathrm{g\,cm}^{-3}$, we cut out the central 8000 AU of the simulation. This leaves us with a rapidly collapsing sphere of gas containing $101.3\,\mathrm{M}_\odot$ and a cosmologically consistent density and velocity structure, which we can use for our initial condition. We use outflow boundary conditions for the hydrodynamics and isolated boundary conditions for the gravity solver. Since the free-fall time of the gas at the boundary of the simulation box is more than three times longer than our maximum simulation run-time, we do not expect this cut-out technique to affect our results much. In fact, at the end of our simulations the gas at the boundaries has barely started to collapse. The initial condition for the magnetic field is identical to Peters et al. (2012), except for the normalization. The magnetic field has a power-law spectrum $P_B(k) \propto k^{3/2}$ on large scales (Kazantsev 1968), peaks on a scale of 1250 AU, corresponding to 20 grid cells in our initial setup, and drops with $P_B(k) \propto k^{-4}$ on smaller scales. This magnetic field spectrum represents an idealization of the spectra measured in collapse simulations by Federrath et al. (2011b).

The temperature field is set by a barotropic equation of

[1] Webpage KROME: http://kromepackage.org/

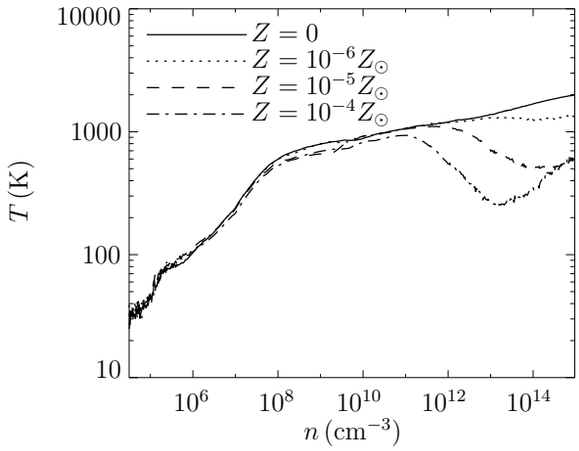

Figure 1. Temperature-density phase diagram for the different metallicities $Z = 0, 10^{-6} Z_\odot, 10^{-5} Z_\odot$ and $10^{-4} Z_\odot$.

state instead of the polytropic equation of state employed by Peters et al. (2012). We use a look-up table generated from the simulations by Dopcke et al. (2013), which include a time-dependent chemical network to model the thermodynamics of a mixture of low-metallicity gas and dust. Figure 1 shows the temperature-density phase diagram for the different metallicities $Z = 0, 10^{-6} Z_\odot, 10^{-5} Z_\odot$ and $10^{-4} Z_\odot$.

For each metallicity, we have run simulations with an initial magnetic field strength of $B_0 = 0$ (Z0B0, Z6B0, Z5B0 and Z4B0 for a metallcity of $Z = 0, 10^{-6} Z_\odot, 10^{-5} Z_\odot$ and $10^{-4} Z_\odot$, respectively) and $B_0 = 10^{-2}\,\mathrm{G}$ (Z0B2, Z6B2, Z5B2 and Z4B2). For $Z = 0$, we have run an additional simulation with $B_0 = 3 \times 10^{-3}\,\mathrm{G}$ (Z0B3). For a summary of the main model parameters, see Table 1. These values have been adopted in order to have a reference case corresponding to the absence of a magnetic field, as well as simulations which start already close to saturation, i.e. where turbulent and magnetic energies are comparable. Such a state is indeed expected due to magnetic field amplification via the small-scale dynamo (Schleicher et al. 2010; Schober et al. 2012a). In the simulations with $B_0 = 10^{-2}\,\mathrm{G}$ ($B_0 = 3 \times 10^{-3}\,\mathrm{G}$), the initial magnetic energy amounts to 45% (4%) of the thermal energy, 11% (2%) of the gravitational energy and 114% (10%) of the kinetic energy of the halo. The simulations with $B_0 = 10^{-2}\,\mathrm{G}$ therefore represent an extreme case where the magnetic field has been maximally amplified.

Since we want to follow all simulations to a similarly high density, the different temperatures at a given density for the various metallicities result in different sizes of the Jeans length and Jeans mass at the resolution limit. We introduce sink particles (Federrath et al. 2010) at a threshold density $n_{\mathrm{thres}} = 10^{15}\,\mathrm{cm}^{-3}$ and set the sink accretion radius to half the Jeans length at this density. The adaptive mesh refinement is set up such that it always resolves the Jeans length during the collapse with at least 32 grid cells and that it resolves the sink particle radius with at least 4 grid cells. Table 1 summarises the parameters and resolution limits of the simulations. We have stopped the simulations when the total cluster mass reached $3.75\,M_\odot$.

3 ANALYSIS

3.1 Magnetic Field Morphology and Filament Formation

Figure 2 shows density slices and magnetic field vectors at three different times during the collapse prior to sink particle formation for the magnetic runs Z0B2, Z6B2, Z5B2 and Z4B2. The figure shows that the magnetic field morphology and the formation of filaments by turbulence during the collapse depends critically on the thermodynamics. In agreement with our findings from more idealised simulations with a constant polytropic exponent (Peters et al. 2012), we observe a virialised, central core and tangled magnetic field vectors as long as the equation of state is super-isothermal, but notice strong shocks with sharp density contrasts and coherent magnetic field vectors on scales much larger than the Jeans volume during isothermal or even sub-isothermal collapse phases. Sub-isothermal collapse occurs in simulations with $Z = 10^{-5} Z_\odot$ and $Z = 10^{-4} Z_\odot$ at densities above $n \gtrsim 10^{12}\,\mathrm{cm}^{-3}$ and $n \gtrsim 10^{11}\,\mathrm{cm}^{-3}$, respectively. The simulations with $Z = 0$ and $Z = 10^{-6} Z_\odot$ are only slightly super-isothermal for $n \gtrsim 10^{8}\,\mathrm{cm}^{-3}$, and so the differences in the qualitative behaviour of the simulations becomes smaller as the collapse proceeds.

3.2 Sink Particle Formation

Figure 3 shows density slices and magnetic field vectors for the three simulations with $Z = 0$. The runs with $Z > 0$ behave similarly and are displayed in Appendix A for the sake of completeness. In all cases, sink particles form in disc-like, rotating structures at the densest parts of filamentary density enhancements. These flattened, rotationally supported structures are called pseudo-discs (Galli & Shu 1993a,b). Their velocity fields can deviate significantly from Keplerian profiles as a result of strong gravitational instability (e.g. Peters et al. 2011). For $Z \leqslant 10^{-6} Z_\odot$, these pseudo-discs appear to be more stable to fragmentation compared to the simulations with $Z \geqslant 10^{-5} Z_\odot$, where sink particle formation and shocks destroy the central, dense structure and sink particle formation proceeds along the forming filaments. We stress that in the following, we will use the term "disc" as abbreviation of "rotationally-flattened structure". Our discs should not be confused with thin discs, which are dominated by the gravity field of the star at the centre, and only gradually become unstable as more gas falls onto the disc and cannot be transported inwards fast enough. We neither see coherently rotating velocity fields nor pronounced radial transport in these discs.

We note that, since we scale the magnetic field vectors by $(\rho/\rho_{\mathrm{s}})^{2/3}$ with a reference density ρ_{s} to visualise the magnetic field over several orders of magnitude in density, very long arrows can originate from areas with a density much lower than ρ_{s} if the magnetic field is comparatively strong there. Therefore, for fixed ρ_{s}, larger arrows mean greater magnetic field amplification beyond pure flux freezing.

Gravoturbulent fragmentation at the sites of sink particle formation is so strong that a coherent disc magnetic field cannot build up. The only exception are runs Z0B3 and Z0B2, in which the most pronounced disc structures form. We have followed the evolution of these disks for roughly

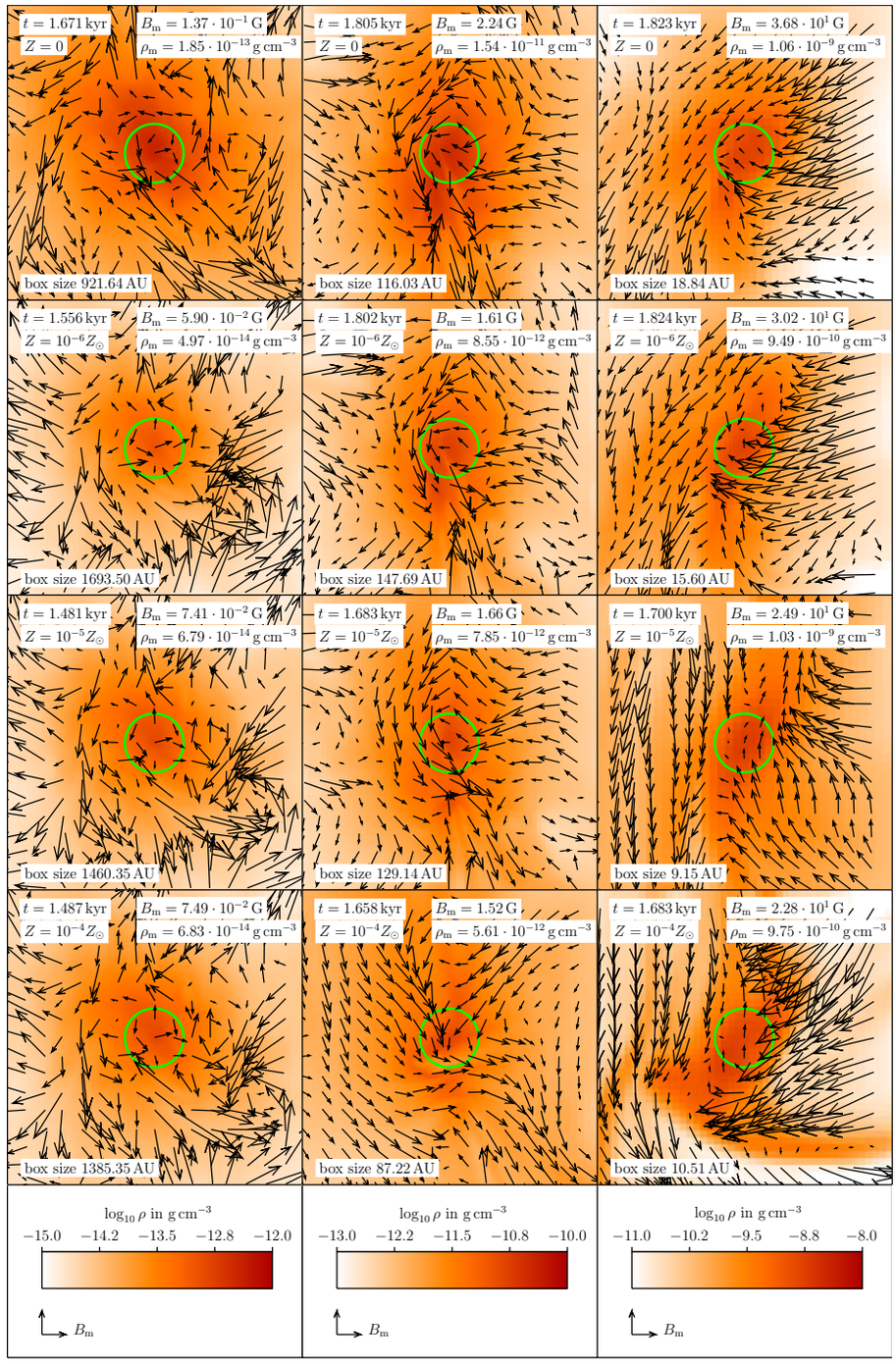

Figure 2. Magnetic field and density structure for the runs Z0B2, Z6B2, Z5B2 and Z4B2 as a function of time. Rows are different metallicities ($Z = 0, 10^{-6}, 10^{-5}, 10^{-4} Z_\odot$, from top to bottom), columns are different times (time advances from left to right). The mean magnetic field B_m and mean density ρ_m within the Jeans volume are indicated in each panel. The magnetic field vectors have been rescaled for plotting by $(\rho/\rho_\mathrm{m})^{2/3}$, and a field strength of B_m at a density of ρ_m corresponds to an arrow of the length given in the legend. The green circle marks the Jeans volume.

Table 1. Simulations

Name	Z ($Z_\odot$)	B_0 (G)	$r_{\rm acc}$ (AU)	$M_{\rm Jeans}$ ($10^{-2} M_\odot$)	N	$M_{\rm mean}$ ($M_\odot$)	$M_{\rm median}$ ($M_\odot$)	σ_M^2 ($M_\odot$)	$t_{\rm first}$ (kyr)	$\dot{M}_{\rm mean}$ ($10^{-3} M_\odot\,{\rm yr}^{-1}$)
Z0B0	0	0	1.63	7.12	4	0.94	1.13	0.20	1.84	10.1
Z0B3	0	3×10^{-3}	1.63	7.12	3	1.25	1.15	0.85	1.83	8.51
Z0B2	0	10^{-2}	1.63	7.12	1	3.75	—	—	1.83	14.6
Z6B0	10^{-6}	0	1.31	3.73	11	0.34	0.21	0.10	1.84	4.42
Z6B2	10^{-6}	10^{-2}	1.31	3.73	6	0.63	0.71	0.07	1.83	6.77
Z5B0	10^{-5}	0	0.89	1.17	13	0.29	0.17	0.08	1.72	3.90
Z5B2	10^{-5}	10^{-2}	0.89	1.17	11	0.34	0.37	0.11	1.70	3.37
Z4B0	10^{-4}	0	0.93	1.32	19	0.20	0.07	0.06	1.70	2.07
Z4B2	10^{-4}	10^{-2}	0.93	1.32	11	0.34	0.32	0.11	1.69	2.87

Metallicity Z, initial magnetic field B_0, sink accretion radius $r_{\rm acc}$ and Jeans mass at the resolution limit $M_{\rm Jeans}$ for the different simulations as well as the number of stars N, the mean mass $M_{\rm mean}$, median mass $M_{\rm median}$ and the variance of the mass spectrum σ_M^2 after approximately $3.75\,M_\odot$ have been accreted onto stars, the time at which the first sink particle forms measured from the beginning of the simulation $t_{\rm first}$ and the average sink accretion rate over the simulation run-time $\dot{M}_{\rm mean}$.

5 and 10 orbital times, respectively. Nevertheless, we found no evidence for magnetically-driven outflows in our simulations. This is probably because we would need to simulate more orbital times to allow a strong toroidal magnetic field to build up.

It is obvious that the magnetic field reduces fragmentation and sink particle formation for all metallicities (compare Table 1). The extreme case is run Z0B2, in which only a single fragment forms in the centre of the disc during the simulation run-time. Hence, although our sink particles do not represent finished stars, we expect the magnetic fields to shift the primordial stellar mass spectrum towards higher masses, similarly to the situation in present-day star formation (e.g. Wang et al. 2010; Peters et al. 2011; Hennebelle et al. 2011; Commerçon et al. 2011; Myers et al. 2013).

Table 1 displays some basic statistical information about the sink particles that form in the different simulations. We show the total number of stars N that form during the simulation as well as the mean mass $M_{\rm mean}$, median mass $M_{\rm median}$ and the variance of the mass spectrum σ_M^2 when the simulations are stopped. Furthermore, we indicate the time $t_{\rm first}$ when the first sink particle forms and the average sink accretion rate $\dot{M}_{\rm mean}$, which is defined as the total mass in sinks at the end of the simulation divided by the cluster age and the number of sink particles.

3.3 Support Functions

We can quantify the relative importance of thermal, turbulent and magnetic support against gravitational collapse using analytical methods introduced by Schmidt et al. (2013). For a gas with thermal pressure P, density ρ, velocity $\boldsymbol{v}$ and magnetic field $\boldsymbol{B}$, we define the thermal support function

$$\Lambda_{\rm therm} = -\frac{1}{\rho}\frac{\partial^2 P}{\partial x_i \partial x_i} + \frac{1}{\rho^2}\frac{\partial \rho}{\partial x_i}\frac{\partial P}{\partial x_i}, \tag{1}$$

the turbulent support function

$$\Lambda_{\rm turb} = \frac{1}{2}\left(\omega_i\omega_i - \sqrt{2S_{ij}S_{ij}}\right) \tag{2}$$

with the vorticity $\boldsymbol{\omega} = \nabla \times \boldsymbol{v}$ and rate-of-strain tensor

$$S_{ij} = \frac{1}{2}\left(\frac{\partial v_i}{\partial x_j} + \frac{\partial v_j}{\partial x_i}\right), \tag{3}$$

and the magnetic support function

$$\begin{aligned}\Lambda_{\rm magn} = {} & \frac{1}{4\pi\rho}\left[-\frac{\partial^2}{\partial x_i \partial x_i}\left(\frac{1}{2}B^2\right) + \frac{\partial B_i}{\partial x_j}\frac{\partial B_j}{\partial x_i}\right] \\ & + \frac{1}{4\pi\rho^2}\frac{\partial \rho}{\partial x_i}\left[\frac{\partial}{\partial x_i}\left(\frac{1}{2}B^2\right) - B_j\frac{\partial B_i}{\partial x_j}\right].\end{aligned} \tag{4}$$

Here we have implicitly assumed summation over repeated indices. Positive values of $\Lambda_{\rm therm}$, $\Lambda_{\rm turb}$ and $\Lambda_{\rm magn}$ indicate support against gravitational collapse, whereas negative values mean that collapse is promoted. As a measure of the contribution to the (positive or negative) support against gravity, we use the ratio of these support functions and the gravitational compression rate $4\pi G\rho$. Thus, we consider the quantities $\Xi_{\rm therm} = \Lambda_{\rm therm}/4\pi G\rho$, $\Xi_{\rm turb} = \Lambda_{\rm turb}/4\pi G\rho$ and $\Xi_{\rm magn} = \Lambda_{\rm magn}/4\pi G\rho$. We compute $\Xi_{\rm therm}$, $\Xi_{\rm turb}$ and $\Xi_{\rm magn}$ for all grid cells and then derive mass-weighted averages for 50 density bins.

Figure 4 shows $\Xi_{\rm therm}$, $\Xi_{\rm turb}$ and $\Xi_{\rm magn}$ as a function of density for the runs with $Z = 0$. The corresponding plots for $Z > 0$ are deferred to Appendix B. Positive and negative values are plotted separately. Especially in run Z0B2, the presence of the magnetic field dramatically enhances not only the magnetic support function, but also the turbulent support function. In the simulations without magnetic fields, the strongest positive support is due to the thermal pressure, while turbulence provides a predominantly negative support due to compressive motions (see similar results by Latif et al. (2013a) and Latif et al. (2014) for a primordial collapse in the presence of strong radiative backgrounds).

In the presence of a magnetic field, the positive and negative contributions are nearly equal over a wide range of densities, with the exception of the highest densities. In contrast, Schmidt et al. (2013) find pronounced positive support by magnetic fields. However, there are important differences compared to the scenario we consider here. Firstly, Schmidt et al. (2013) compute the support for turbulence produced by external forcing in a periodic box, where gravitational

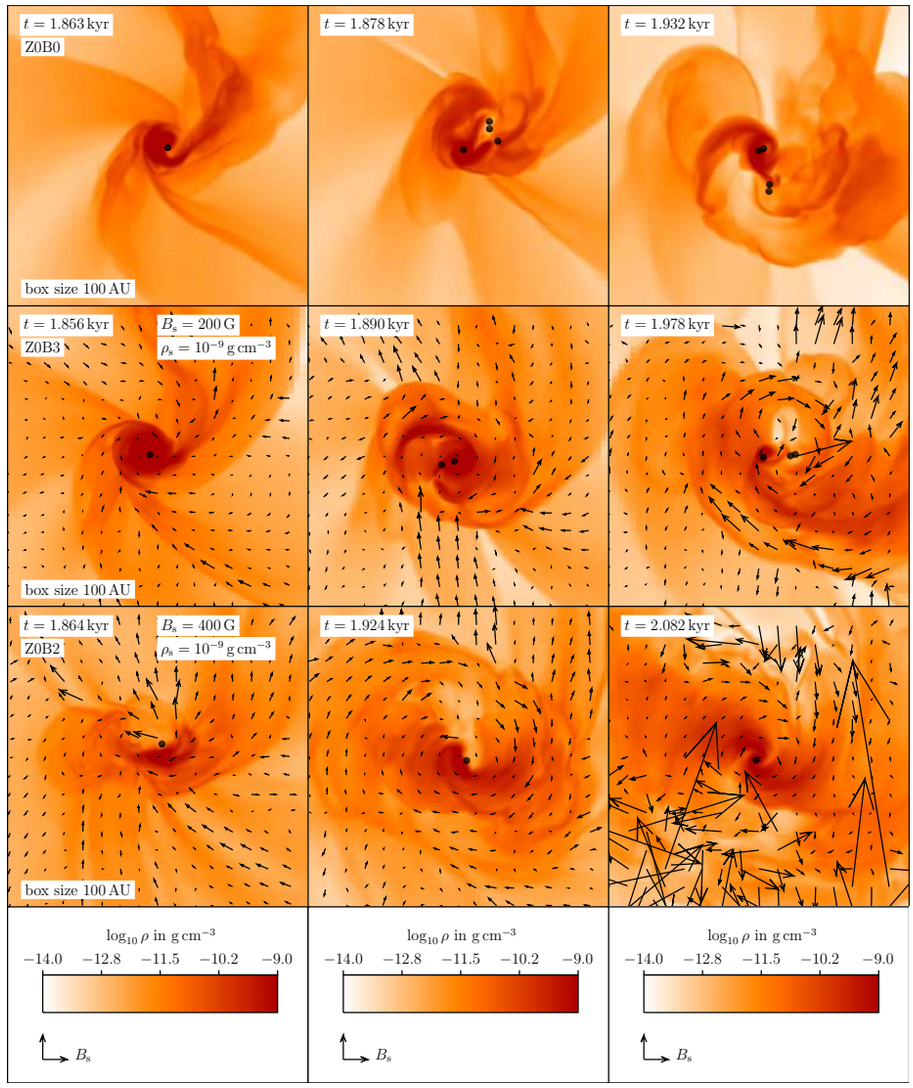

Figure 3. Magnetic field and density structure for the runs Z0B0, Z0B3 and Z0B2 as a function of time. Rows are different initial magnetic field strengths ($B_0 = 0, 3 \cdot 10^{-3}, 10^{-2}$ G, from top to bottom), columns are different times (time advances from left to right). The snapshots show the simulations when the cluster masses have reached 1, 2 and 3.75 $M_\odot$, respectively. The magnetic field vectors have been rescaled for plotting by $(\rho/\rho_\mathrm{s})^{2/3}$, and a field strength of B_s at a density of ρ_s corresponds to an arrow of the length given in the legend. Black dots represent sink particles.

collapse is triggered by supersonic turbulent compressions of the gas. Secondly, no sink particles are inserted in their simulations. As a result, the magnetic field is squeezed into collapsing gas of arbitrarily high density. In our simulations, on the other hand, the magnetic field is decoupled from the collapsing gas once sink particles are inserted. This limits somewhat the maximal magnetic pressure that can build up against gravity. Thirdly, we expect our collapsing halo to have a stronger tendency to produce disc-like structures in comparison to turbulence produced by random forcing, which, averaged over the box, induces zero angular momentum. These rotating discs might affect the field morphology dramatically by winding up magnetic field lines and building up magnetic pressure. Nevertheless, we see that the net magnetic support becomes positive at densities of $10^{-9} - 10^{-10}$ g cm^{-3}, where a protostellar accretion disc has formed. This effect is particularly pronounced in the simulation Z0B2, but also visible in Z0B3 with a weaker magnetic field, as well as in the higher-metallicity simulations. Within the disc, the magnetic field therefore provides a stabilising contribution, as also reported by Latif et al. (2014). We therefore expect that the fragmentation timescale increases in the presence of a magnetic field, as supported by a more detailed analysis of the relevant timescales in the system (Section 3.6).

3.4 Angular Momentum

Figure 5 displays the specific angular momentum j_z at the time of first sink formation as a function of radius and en-

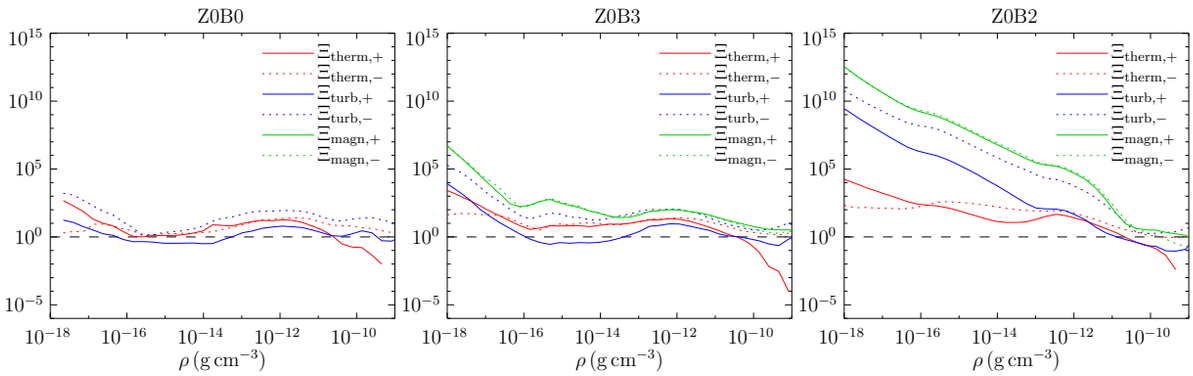

Figure 4. Support functions as a function of density after accretion of 3.75 $M_\odot$ for runs Z0B0, Z0B3 and Z0B2.

closed mass for all simulations. The values shown are the mass-weighted averages over spherical shells centred on the densest grid cell in the domain. Differences between the profiles are very small in general, so that even a magnetic field close to saturation does not seem to substantially impact the specific angular momentum profile. The magnetised halos have only a slightly larger j_z in the inner 100 AU. This behaviour is to be expected for the runs with $Z = 0$, because here the disc structure, which is aligned approximately orthogonally to the z-axis of the simulation grid, becomes much more pronounced when the magnetic field increases, but for $Z > 0$ it is less clear from the density structures how an enhanced j_z can be interpreted. The other components of the specific angular momentum vector, j_x and j_y, have more complicated, non-monotonic profiles, and show no strong trend with metallicity or magnetic field strength. In particular, both j_x and j_y change signs several times as a function of radius, so that the situation gets very difficult to visualise.

In their collapse simulations, Machida & Doi (2013) find that magnetic braking transports angular momentum very efficiently and prevents the formation of a disc when $B \gtrsim 10^{-12}(n/1\,\mathrm{cm^{-3}})^{-2/3}\,\mathrm{G}$, which is of a similar magnitude as our initial field strengths. This difference between the two sets of simulations is most likely caused by the differing initial conditions. Machida & Doi (2013) initialise their simulations with large-scale ordered magnetic field configurations, whereas our simulations start from magnetic fields with no global order.

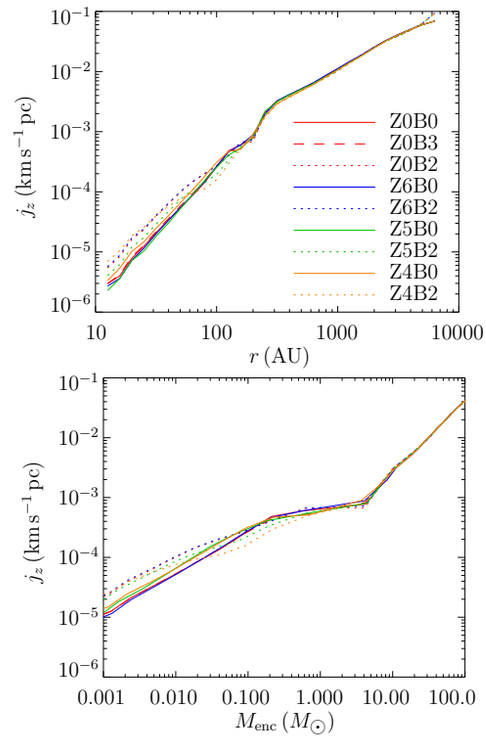

Figure 5. Specific angular momentum j_z for all simulations at the time of first sink formation as function of radius r (*top*) and enclosed mass $M_{\rm enc}$ (*bottom*).

3.5 Mass Spectra

Table 1 summarises the properties of the sink particle mass spectra for the different simulations. In our simulations, the sink particles represent dense collapsing fragments of gas. Such fragments are the very earliest stages of protostars as they have collapsed to high densities but have not yet started to contract to the main sequence. The magnetic field reduces the number of sinks and increases the mean sink mass in all cases. For a fixed magnetic field strength, more sink particles form at a given star formation efficiency with growing metallicity.

The final mass spectra of all simulations are shown in Figure 6. The histograms appear to be flat and show no evidence for a transition in the shape of the initial mass function at $Z = 10^{-4}Z_\odot$ as observed by Dopcke et al. (2013). However, we have accreted 1 $M_\odot$ of gas less in our sink particles than Dopcke et al. (2013) and have limited data points in our sample, so that our results are not statistically significant. What is clear is that in all cases where there is fragmentation a small cluster with a spectrum of fragment masses develops. These fragments will act as seeds which will grow in mass through accretion, possibly mergers, and further fragmentation to form a final stellar cluster. The reduction in the number of fragments in the magnetic case suggests that the final clusters may have fewer stars compared to the non-magnetic case.

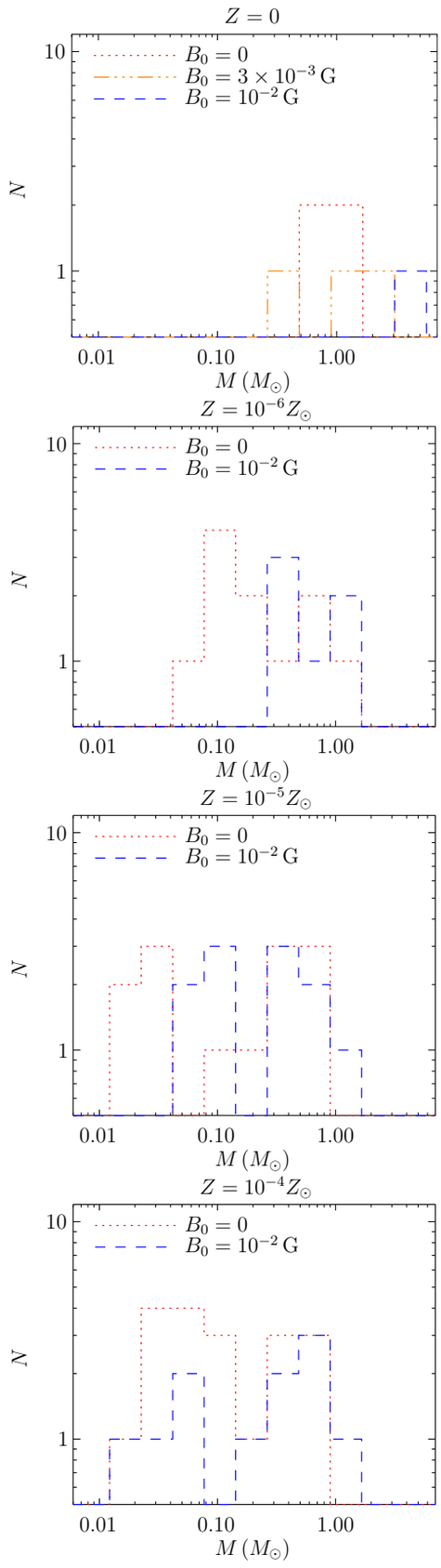

Figure 6. Sink particle mass spectra after approximately $3.75\,M_\odot$ of gas have been accreted onto sinks.

3.6 Timescale Analysis

We try to understand the differences in the mass spectra with a timescale analysis. We define a fragmentation timescale

$$\tau_{\rm frag}(t) = \frac{1}{N(t)} \sum_{i=2}^{N(t)} \Delta t_i, \tag{5}$$

with the number of sink particles $N(t)$ at time t and the time difference Δt_i between the formation of sink particles i and $i-1$. In other words, $\tau_{\rm frag}$ is the cluster age divided by the number of stars. The fragmentation timescale for all simulations as a function of cluster mass is plotted in Figure 7. Since run Z0B2 only forms a single sink particle, our figure for $\tau_{\rm frag}$ must be considered as a lower limit of the true value.

Most simulations have a fragmentation timescale between 1 and 30 yr, but $\tau_{\rm frag}$ for the non-fragmenting run Z0B2 is almost 10 times larger than this. In this scenario, the disc is particularly stable, as also shown through the analysis of the support functions in Section 3.3. In all cases, $\tau_{\rm frag}$ is greater in the magnetic than in the purely hydrodynamic simulations, typically by about a factor of 3. In the primordial simulation without magnetic fields, the fragmentation timescale is enhanced by a factor of at least 10 compared to the runs with $Z > 0$. However, the fragmentation timescale appears to depend very weakly on Z for $Z > 0$. Magnetic fields typically increase it by a factor of 3, and indeed, the fragmentation timescale in $Z > 0$ runs with magnetic fields is comparable to the $Z = 0$ run with no magnetic field.

We compare $\tau_{\rm frag}$ with an accretion timescale defined as

$$\tau_{\rm acc}(t) = \frac{M(t)}{\dot{M}(t)} \tag{6}$$

with the total mass of the cluster M and the total accretion rate onto the cluster $\dot{M}$. The accretion timescale is shown in Figure 7 as well. Again, magnetised simulations have greater accretion timescales on average than non-magnetic runs.

The ratio of $\tau_{\rm frag}$ and $\tau_{\rm acc}$ is plotted in Figure 8. This ratio is smaller than unity on average and decreases with time. This means that $\tau_{\rm acc}$ grows faster than $\tau_{\rm frag}$ as the stellar cluster grows. In other words, the stellar system effectively decouples from the supply of gas from the environment. The central star-forming region is so unstable to gravitational collapse that further accretion of gas from the halo is not necessary to maintain the star formation activity. Run Z0B2 is the only simulation for which $\tau_{\rm frag}/\tau_{\rm acc}$ does not decrease but oscillates around unity. The extraordinary stability of the disc in run Z0B2 is consistent with the unusually large support functions for this simulation (compare Figure 4).

4 DISCUSSION

In this paper, we present a study assessing the relative impact of metals and magnetic fields during low-metallicity star formation. For this purpose, we consider metallicities ranging from the primordial case ($Z = 0$) up to metallicities of $10^{-4}\ Z_\odot$. The magnetic field strength has been chosen such that the magnetic energy becomes comparable to

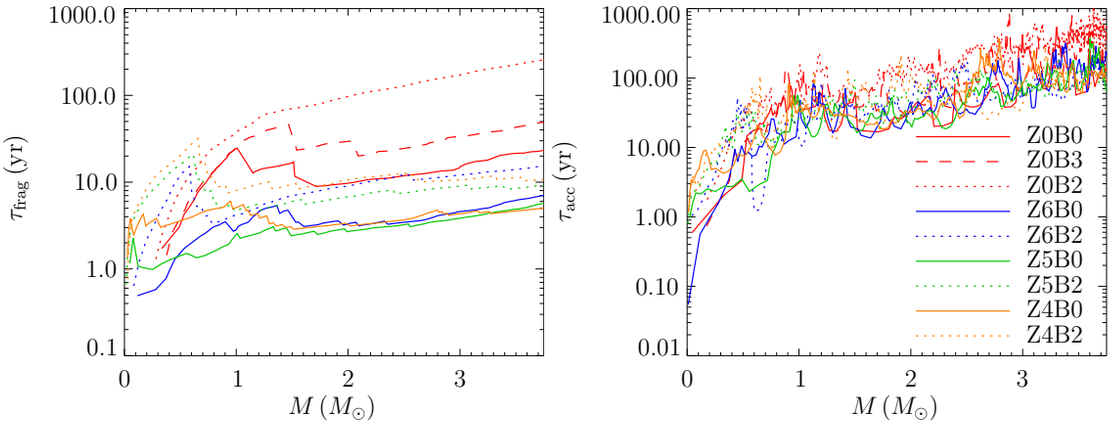

Figure 7. Fragmentation timescale $\tau_{\rm frag}$ (*left*) and accretion timescale $\tau_{\rm acc}$ (*right*) as a function of cluster mass for all simulations.

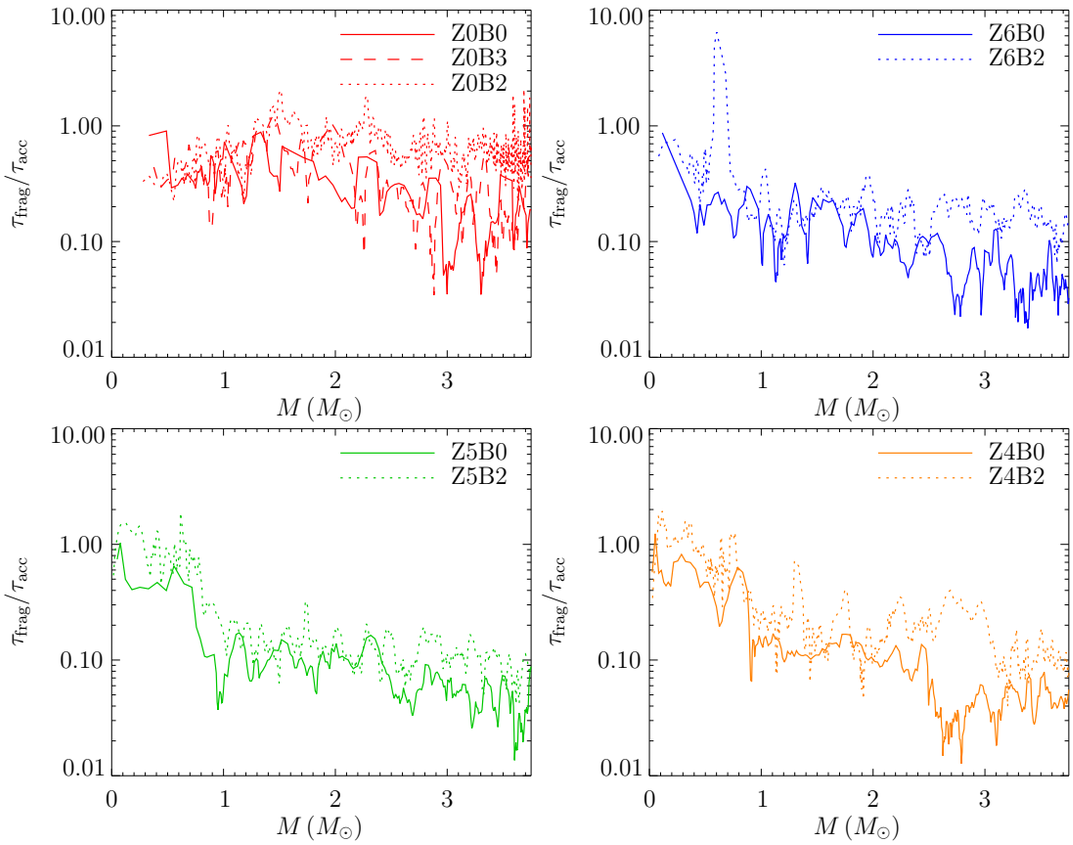

Figure 8. Ratio $\tau_{\rm frag}/\tau_{\rm acc}$ as a function of cluster mass for all simulations.

the turbulent energy during the formation of the disc, as expected through the operation of the small-scale dynamo (Schleicher et al. 2010; Schober et al. 2012a). We further pursue comparison runs with no magnetic fields to quantify their dynamical impact. In all cases, we follow the collapse until 3.75 $M_\odot$ of gas are converted into sink particles.

In the runs without magnetic fields, we find that the primordial simulation provides the most stable configuration, where the fragmentation timescale $\tau_{\rm frag}$ is enhanced by a factor of ~ 10 compared to the higher-metallicity runs. For $Z > 0$, however, we observe that $\tau_{\rm frag}$ depends only weakly on the actual metallicity. The accretion timescale $\tau_{\rm acc}$ of the cluster is slightly enhanced in the primordial case, but not as much as $\tau_{\rm frag}$, and overall $\tau_{\rm acc}$ appears to depend only weakly on metallicity. We therefore conclude that the overall accretion is set by the dynamics of the global collapse and therefore insensitive to the cooling at high densities.

In the presence of magnetic fields, the primordial disc becomes very stable, and $\tau_{\rm frag}$ increases by a factor of at least 10. Up to the time covered in our simulation ($\sim 2\,$kyr), only one sink particle has formed. For $Z > 0$, $\tau_{\rm frag}$ is still enhanced by a factor of 3, but fragmentation is no longer

suppressed. We find, however, a similarity between primordial runs without magnetic fields, and low-metallicity runs with magnetic fields, which have comparable fragmentation timescales.

These results are explored using the thermal, turbulent and magnetic support functions proposed by Schmidt et al. (2013). In the absence of magnetic fields, the thermal pressure yields the dominant positive support for all metallicities explored here, while turbulence yields predominantly negative contributions due to the presence of compressible motions. On large scales where collapse has already occured, magnetic fields have comparable negative and positive contributions, while they act as a stabilising agent on the small scale of the protostellar disc. The latter explains why the fragmentation timescale increases in the presence of magnetic fields.

Finally, we assess the impact of these processes on the sink particle mass functions. These sink particles represent collapsing fragments, not finished stars. At the time when we stop our simulation, i.e. when 3.75 $M_\odot$ are converted into sinks, we compare the sink particle mass distribution in simulations of different metallicities and with and without magnetic fields. In the primordial run with a saturated magnetic field, only one single fragment forms, therefore indicating a potentially top-heavy sink mass function. With decreasing field strength, the number of sinks slightly increased, but remains reduced compared to the $Z > 0$ simulations. A shift towards larger sink masses is therefore expected in the primordial case, which is particularly pronounced in the presence of magnetic fields.

In the simulations with $Z > 0$, the sink mass function appears rather similar regardless of the actual value of Z or the presence of a magnetic field. We note, however, that the number of sinks is somewhat reduced in all simulations with magnetic fields, and there is a weak trend indicating the formation of slightly more massive sinks. In order to more strongly constrain the potential influence of metallicity and magnetic fields on the stellar initial mass function (IMF), we would need to follow the simulations until a larger number of sinks has formed, therefore improving the statistics for assessing the IMF. However, one should further explore the impact of different initial conditions, and such simulations would also require to include additional physics such as radiative feedback (e.g. Peters et al. 2010a,c,b, 2011; Smith et al. 2011; Stacy et al. 2012). In particular, the data for our barotropic equation of state was extracted from the simulations of Dopcke et al. (2013) before a disc was formed, which probably results in an overestimate of the temperature and too stable discs. On the other hand, our equation of state does not include stellar feedback, which would heat the disc by an unknown amount, stabilising the disc again. Which of these two competing processes dominates is at present unclear. Nevertheless, our results indicate a similarity between metal enrichment and magnetic fields in terms of the fragmentation behaviour, which needs to be explored further in future studies.

ACKNOWLEDGEMENTS

We thank David Collins for technical support and Gustavo Dopcke, Simon Glover and Paul Clark for providing the effective equation of state employed here as well as for stimulating scientific discussions. We also thank the anonymous referee for useful comments that helped to improve the paper. T.P. acknowledges financial support through SNF grant 200020_137896 and a Forschungskredit of the University of Zürich, grant no. FK-13-112. D.R.G.S. and W.S. thank the DFG for funding via the Collaborative Research Center (CRC) 963 on *Astrophysical Flow Instabilities and Turbulence* (projects A12 and A15). D.R.G.S., R.S.K. and R.J.S acknowledge support from the DFG via the SPP 1573 (grants SCHL 1964/1-1, KL 1358/14-1 & SM 321/1-1) and via the SFB 881 *The Milky Way System* (sub-projects B1, B2, B3). R.S.K. further acknowledges support from the Baden-Württemberg Foundation via contract research (grant P-LS-SPII/18) as well as from the European Research Council via the ERC Advanced Grant 'STARLIGHT: Formation of the First Stars' (project ID 339177). We acknowledge computing time at the Leibniz-Rechenzentrum (LRZ) in Garching under project ID h1343, at the Swiss National Supercomputing Centre (CSCS) under project IDs s364/s417 and at Jülich Supercomputing Centre under project ID HHD14. The FLASH code was in part developed by the DOE-supported Alliances Center for Astrophysical Thermonuclear Flashes (ASCI) at the University of Chicago. The data was partly analysed with the yt code (Turk et al. 2011).

REFERENCES

Abel, T., Bryan, G. L., & Norman, M. L. 2002, Science, 295, 93
Arshakian, T. G., Beck, R., Krause, M., & Sokoloff, D. 2009, A&A, 494, 21
Aykutalp, A., & Spaans, M. 2011, ApJ, 737, 63
Barkana, R., & Loeb, A. 2001, Phys. Rep., 349, 125
Biermann, L. 1950, Zeitschrift für Naturforschung, 5A, 65
Bouchut, F., Klingenberg, C., & Waagan, K. 2007, Numerische Mathematik, 108, 7
Bovino, S., Grassi, T., Latif, M. A., & Schleicher, D. R. G. 2013, MNRAS, 434, L36
Bovino, S., Latif, M. A., Grassi, T., & Schleicher, D. R. G. 2014a, arXiv:1402.4403
Bovino, S., Schleicher, D. R. G., & Grassi, T. 2014b, A&A, 561, A13
Brandenburg, A., & Subramanian, K. 2005, Phys. Rep., 417, 1
Bromm, V., Coppi, P. S., & Larson, R. B. 2002, ApJ, 564, 23
Bromm, V., & Loeb, A. 2003, Nature, 425, 812
Caffau, E., Bonifacio, P., François, P., et al. 2011, Nature, 477, 67
—. 2012, A&A, 542, A51
—. 2013, A&A, 560, A15
Cazaux, S., & Spaans, M. 2004, ApJ, 611, 40
—. 2009, A&A, 496, 365
Clark, P. C., Glover, S. C. O., & Klessen, R. S. 2008, ApJ, 672, 757
Clark, P. C., Glover, S. C. O., Klessen, R. S., & Bromm, V. 2011a, ApJ, 727, 110
Clark, P. C., Glover, S. C. O., Smith, R. J., et al. 2011b, Science, 331, 1040

Commerçon, B., Hennebelle, P., & Henning, T. 2011, ApJ, 742, L9
de Souza, R. S., & Opher, R. 2010, Phys. Rev. D, 81, 067301
Dopcke, G., Glover, S. C. O., Clark, P. C., & Klessen, R. S. 2011, ApJ, 729, L3
—. 2013, ApJ, 766, 103
Federrath, C., Banerjee, R., Clark, P. C., & Klessen, R. S. 2010, ApJ, 713, 269
Federrath, C., Chabrier, G., Schober, J., et al. 2011a, Phys. Rev. Lett., 107, 114504
Federrath, C., Sur, S., Schleicher, D. R. G., Banerjee, R., & Klessen, R. S. 2011b, ApJ, 731, 62
Frebel, A., Kirby, E. N., & Simon, J. D. 2010, Nature, 464, 72
Fryxell, B., Olson, K., Ricker, P., et al. 2000, ApJS, 131, 273
Galli, D., & Shu, F. H. 1993a, ApJ, 417, 220
—. 1993b, ApJ, 417, 243
Gnedin, N. Y. 2000, ApJ, 535, 530
Grassi, T., Bovino, S., Schleicher, D. R. G., et al. 2014, MNRAS, 439, 2386
Grasso, D., & Rubinstein, H. R. 2001, Phys. Rep., 348, 163
Greif, T. H., Bromm, V., Clark, P. C., et al. 2012, MNRAS, 424, 399
Greif, T. H., Glover, S. C. O., Bromm, V., & Klessen, R. S. 2010, ApJ, 716, 510
Greif, T. H., Johnson, J. L., Klessen, R. S., & Bromm, V. 2008, MNRAS, 387, 1021
Greif, T. H., Springel, V., White, S. D. M., et al. 2011, ApJ, 737, 75
Hennebelle, P., Commerçon, B., Joos, M., et al. 2011, A&A, 528, A72
Hirano, S., Hosokawa, T., Yoshida, N., et al. 2014, ApJ, 781, 60
Hocuk, S., & Spaans, M. 2010, A&A, 510, A110
Hosokawa, T., Omukai, K., Yoshida, N., & Yorke, H. W. 2011, Science, 334, 1250
Jappsen, A.-K., Glover, S. C. O., Klessen, R. S., & Mac Low, M.-M. 2007, ApJ, 660, 1332
Jappsen, A.-K., Klessen, R. S., Glover, S. C. O., & Mac Low, M.-M. 2009a, ApJ, 696, 1065
Jappsen, A.-K., Mac Low, M.-M., Glover, S. C. O., Klessen, R. S., & Kitsionas, S. 2009b, ApJ, 694, 1161
Kazantsev, A. P. 1968, Sov. Phys. JETP, 26, 1031
Klessen, R. S., Glover, S. C. O., & Clark, P. C. 2012, MNRAS, 421, 3217
Latif, M. A., Schleicher, D. R. G., & Schmidt, W. 2014, MNRAS, 440, 1551
Latif, M. A., Schleicher, D. R. G., Schmidt, W., & Niemeyer, J. 2013a, MNRAS, 433, 1607
—. 2013b, MNRAS, 436, 2989
—. 2013c, ApJ, 772, L3
—. 2013d, MNRAS, 432, 668
Latif, M. A., Schleicher, D. R. G., & Spaans, M. 2012, A&A, 540, A101
Li, Y., Klessen, R. S., & Mac Low, M.-M. 2003, ApJ, 592, 975
Machida, M. N., & Doi, K. 2013, MNRAS, 435, 3283
Machida, M. N., Matsumoto, T., & Inutsuka, S.-i. 2008, ApJ, 685, 690
Machida, M. N., Omukai, K., Matsumoto, T., & Inutsuka, S.-i. 2006, ApJ, 647, L1
Myers, A. T., McKee, C. F., Cunningham, A. J., Klein, R. I., & Krumholz, M. R. 2013, ApJ, 766, 97
Omukai, K., Schneider, R., & Haiman, Z. 2008, ApJ, 686, 801
Omukai, K., Tsuribe, T., Schneider, R., & Ferrara, A. 2005, ApJ, 626, 627
Peters, T., Banerjee, R., Klessen, R. S., & Mac Low, M.-M. 2011, ApJ, 729, 72
Peters, T., Banerjee, R., Klessen, R. S., et al. 2010a, ApJ, 711, 1017
Peters, T., Klessen, R. S., Mac Low, M.-M., & Banerjee, R. 2010b, ApJ, 725, 134
Peters, T., Mac Low, M.-M., Banerjee, R., Klessen, R. S., & Dullemond, C. P. 2010c, ApJ, 719, 831
Peters, T., Schleicher, D. R. G., Klessen, R. S., et al. 2012, ApJ, 760, L28
Pudritz, R. E., & Silk, J. 1989, ApJ, 342, 650
Ritter, J. S., Safranek-Shrader, C., Gnat, O., Milosavljević, M., & Bromm, V. 2012, ApJ, 761, 56
Safranek-Shrader, C., Bromm, V., & Milosavljević, M. 2010, ApJ, 723, 1568
Safranek-Shrader, C., Milosavljević, M., & Bromm, V. 2014a, MNRAS, 440, L76
—. 2014b, MNRAS, 438, 1669
Salvadori, S., Ferrara, A., Schneider, R., Scannapieco, E., & Kawata, D. 2010, MNRAS, 401, L5
Schekochihin, A. A., Cowley, S. C., Hammett, G. W., Maron, J. L., & McWilliams, J. C. 2002, New Journal of Physics, 4, 84
Schleicher, D. R. G., Banerjee, R., & Klessen, R. S. 2008, Phys. Rev. D, 78, 083005
Schleicher, D. R. G., Banerjee, R., Sur, S., et al. 2010, A&A, 522, A115
Schleicher, D. R. G., Schober, J., Federrath, C., Bovino, S., & Schmidt, W. 2013, New Journal of Physics, 15, 023017
Schlickeiser, R. 2012, Phys. Rev. Lett., 109, 261101
Schlickeiser, R., & Felten, T. 2013, ApJ, 778, 39
Schmidt, W., Collins, D. C., & Kritsuk, A. G. 2013, MNRAS, 431, 3196
Schneider, R., Ferrara, A., Salvaterra, R., Omukai, K., & Bromm, V. 2003, Nature, 422, 869
Schneider, R., Omukai, K., Limongi, M., et al. 2012, MNRAS, 423, L60
Schober, J., Schleicher, D., Federrath, C., et al. 2012a, ApJ, 754, 99
Schober, J., Schleicher, D., Federrath, C., Klessen, R., & Banerjee, R. 2012b, PRE, 85, 026303
Seifried, D., Banerjee, R., & Schleicher, D. 2014, MNRAS, 440, 24
Shapiro, P. R., Giroux, M. L., & Babul, A. 1994, ApJ, 427, 25
Shiromoto, Y., Susa, H., & Hosokawa, T. 2014, ApJ, 782, 108
Silk, J., & Langer, M. 2006, MNRAS, 371, 444
Smith, B. D., Turk, M. J., Sigurdsson, S., O'Shea, B. W., & Norman, M. L. 2009, ApJ, 691, 441
Smith, R. J., Glover, S. C. O., Clark, P. C., Greif, T., & Klessen, R. S. 2011, MNRAS, 414, 3633
Stacy, A., & Bromm, V. 2014, ApJ, 785, 73
Stacy, A., Greif, T. H., & Bromm, V. 2010, MNRAS, 403, 45
—. 2012, MNRAS, 422, 290

Sur, S., Federrath, C., Schleicher, D. R. G., Banerjee, R., & Klessen, R. S. 2012, MNRAS, 423, 3148
Sur, S., Schleicher, D. R. G., Banerjee, R., Federrath, C., & Klessen, R. S. 2010, ApJ, 721, L134
Susa, H. 2013, ApJ, 773, 185
Tan, J. C., & Blackman, E. G. 2004, ApJ, 603, 401
Turk, M. J., Oishi, J. S., Abel, T., & Bryan, G. L. 2012, ApJ, 745, 154
Turk, M. J., Smith, B. D., Oishi, J. S., et al. 2011, ApJS, 192, 9
Waagan, K. 2009, J. Comput. Phys., 228, 8609
Wang, P., Li, Z.-Y., Abel, T., & Nakamura, F. 2010, ApJ, 709, 27
Wise, J. H., Turk, M. J., Norman, M. L., & Abel, T. 2012, ApJ, 745, 50
Yoshida, N., Omukai, K., & Hernquist, L. 2008, Science, 321, 669

APPENDIX A: MAGNETIC FIELD AND DENSITY STRUCTURE FOR SIMULATIONS WITH $Z > 0$

In this Appendix, we show the density structures and magnetic field vectors for the simulations with $Z = 10^{-6} Z_\odot$ (Figure A1), $Z = 10^{-5} Z_\odot$ (Figure A2) and $Z = 10^{-4} Z_\odot$ (Figure A3) as the sink particles form. The structues look very similar by and large, but the filaments seem to be more pronounced than in the completely metal-free case $Z = 0$ (Figure 3).

APPENDIX B: SUPPORT FUNCTIONS FOR SIMULATIONS WITH $Z > 0$

Here we show plots of $\Xi_{\rm therm}$, $\Xi_{\rm turb}$ and $\Xi_{\rm magn}$ for the runs with $Z = 10^{-6} Z_\odot$ (Figure B1), $Z = 10^{-5} Z_\odot$ (Figure B2) and $Z = 10^{-4} Z_\odot$ (Figure B3). There is no strong variation with metallicity in general. However, the simulation Z0B2 (Figure 4) has significantly larger support functions than all runs with $Z > 0$, which explains the reduced fragmentation observed in run Z0B2.

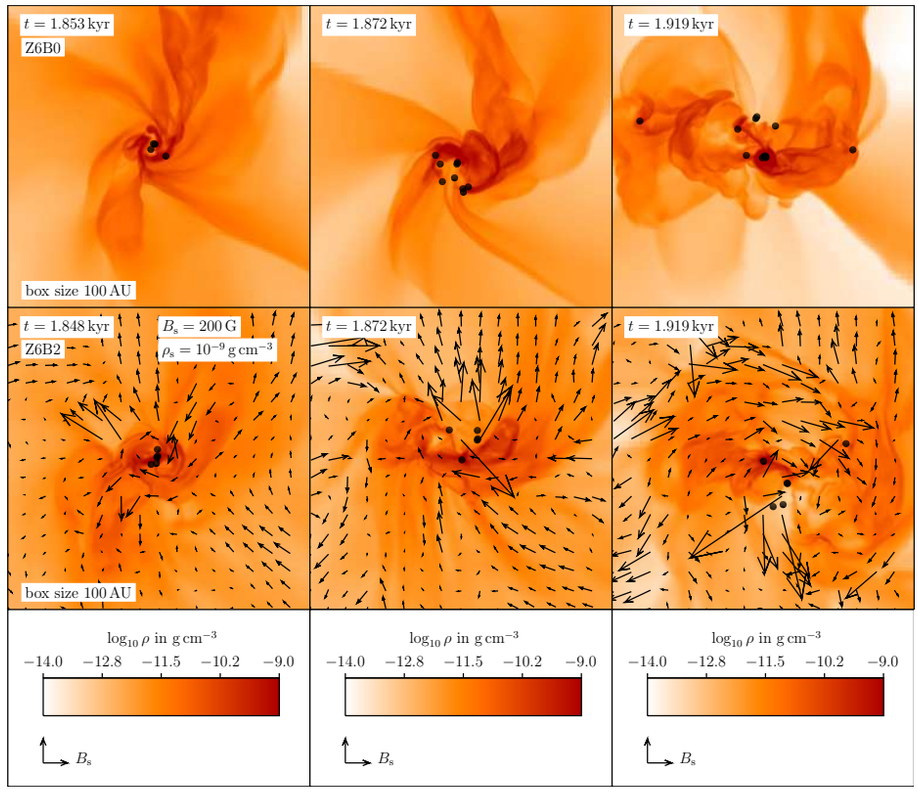

Figure A1. Magnetic field and density structure for the runs Z6B0 and Z6B2 as a function of time. Rows are different initial magnetic field strengths ($B_0 = 0, 10^{-2}$ G, from top to bottom), columns are different times (time advances from left to right). The snapshots show the simulations when the cluster masses have reached 1, 2 and 3.75 $M_\odot$, respectively. The magnetic field vectors have been rescaled for plotting by $(\rho/\rho_\mathrm{s})^{2/3}$, and a field strength of B_s at a density of ρ_s corresponds to an arrow of the length given in the legend. Black dots represent sink particles.

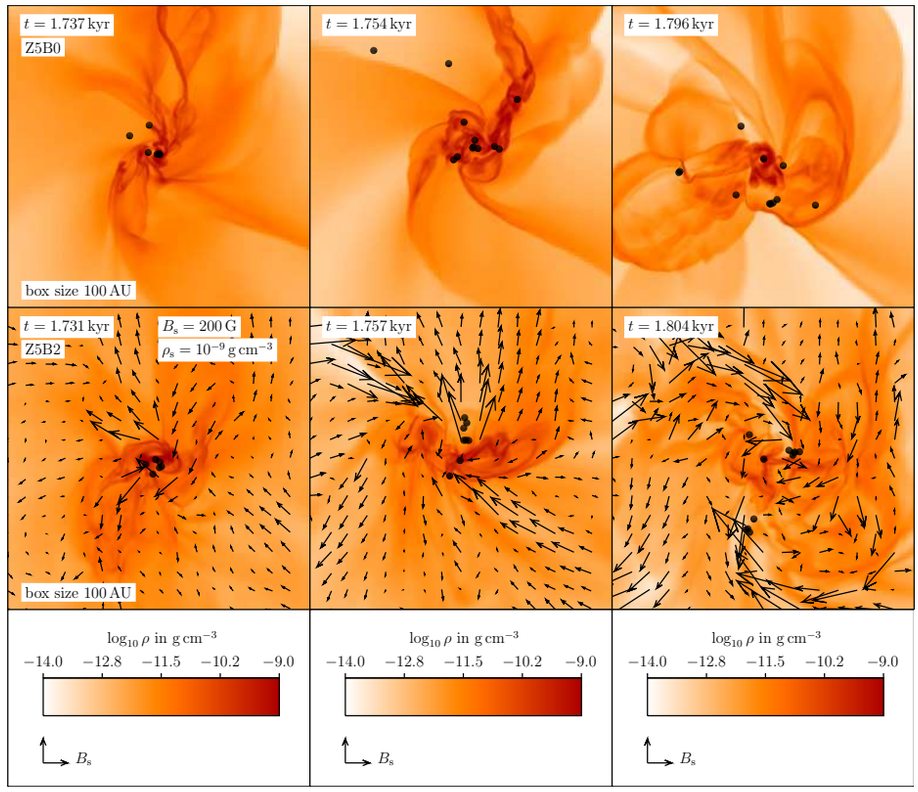

Figure A2. Magnetic field and density structure for the runs Z5B0 and Z5B2 as a function of time. Rows are different initial magnetic field strengths ($B_0 = 0, 10^{-2}$ G, from top to bottom), columns are different times (time advances from left to right). The snapshots show the simulations when the cluster masses have reached 1, 2 and 3.75 $M_\odot$, respectively. The magnetic field vectors have been rescaled for plotting by $(\rho/\rho_\mathrm{s})^{2/3}$, and a field strength of B_s at a density of ρ_s corresponds to an arrow of the length given in the legend. Black dots represent sink particles.

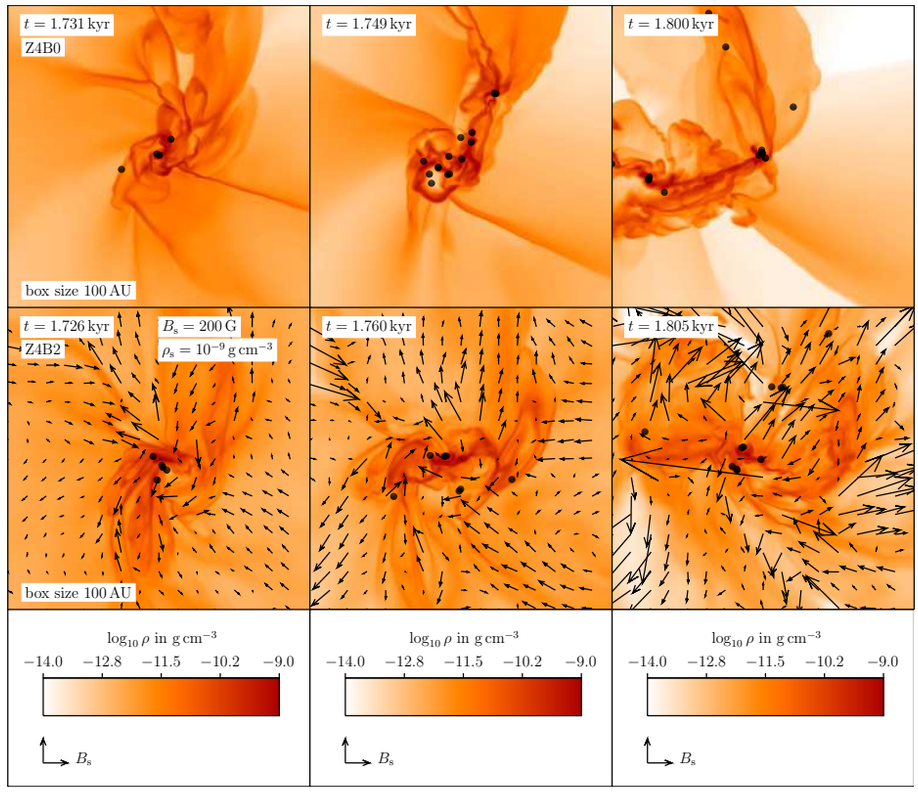

Figure A3. Magnetic field and density structure for the runs Z4B0 and Z4B2 as a function of time. Rows are different initial magnetic field strengths ($B_0 = 0, 10^{-2}$ G, from top to bottom), columns are different times (time advances from left to right). The snapshots show the simulations when the cluster masses have reached 1, 2 and 3.75 $M_\odot$, respectively. The magnetic field vectors have been rescaled for plotting by $(\rho/\rho_s)^{2/3}$, and a field strength of B_s at a density of ρ_s corresponds to an arrow of the length given in the legend. Black dots represent sink particles.

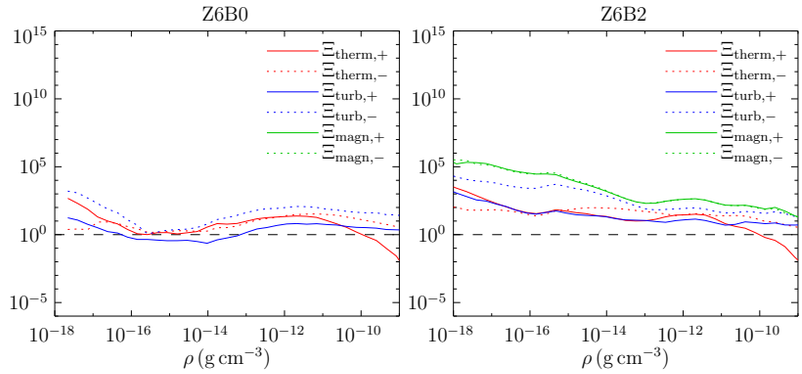

Figure B1. Support functions as a function of density after accretion of 3.75 $M_\odot$ for runs Z6B0 and Z6B2.

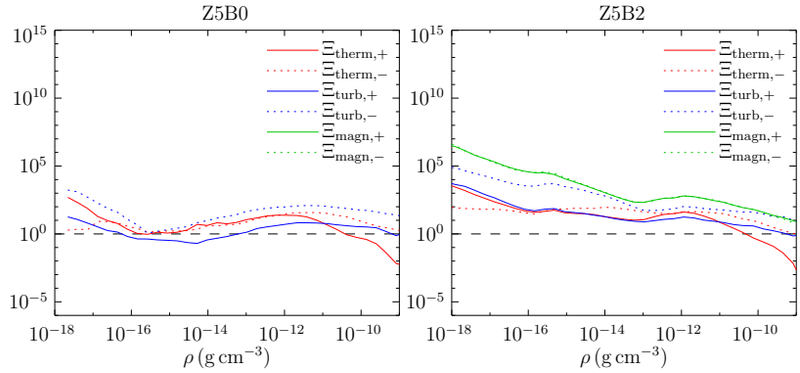

Figure B2. Support functions as a function of density after accretion of 3.75 $M_\odot$ for runs Z5B0 and Z2B2.

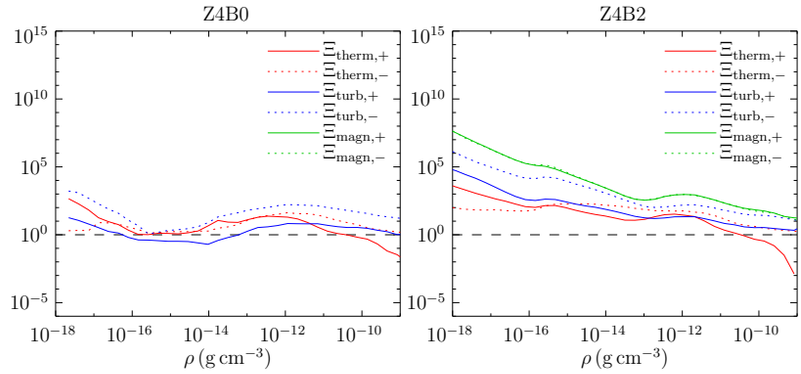

Figure B3. Support functions as a function of density after accretion of 3.75 $M_\odot$ for runs Z4B0 and Z4B2.